

Novel $z \sim 10$ auroral line measurements extend the gradual offset of the FMR deep into the first Gyr of cosmic time

Clara L. Pollock^{1,2}, Rashmi Gottumukkala^{1,2}, Kasper E. Heintz^{1,2,3}, Gabriel B. Brammer^{1,2}, Guido Roberts-Borsani⁴, Pascal A. Oesch^{3,1,2}, Joris Witstok^{1,2}, Karla Z. Arellano-Córdova⁵, Fergus Cullen⁵, Dirk Scholte⁵, Chamilla Terp^{1,2}, Lucie Rowland⁶, Albert Sneppen^{1,2}, Kei Ito^{1,7}, Francesco Valentino^{1,7}, Jorrit Matthee⁸, Darach Watson^{1,2}, and Sune Toft^{1,2}

¹ Cosmic Dawn Center (DAWN), Denmark

² Niels Bohr Institute, University of Copenhagen, Jagtvej 128, 2200 Copenhagen N, Denmark

³ Department of Astronomy, University of Geneva, Chemin Pegasi 51, 1290 Versoix, Switzerland

⁴ Department of Physics & Astronomy, University College London, London, WC1E 6BT, UK

⁵ Institute for Astronomy, University of Edinburgh, Royal Observatory, Edinburgh, EH9 3HJ, UK

⁶ Leiden Observatory, Leiden University, P.O. Box 9513, NL-2300 RA Leiden, the Netherlands

⁷ DTU Space, Technical University of Denmark, Elektrovej 327, DK2800 Kgs. Lyngby, Denmark

⁸ Institute of Science and Technology Austria (ISTA), Am Campus 1, 3400 Klosterneuburg, Austria

June 2025

ABSTRACT

The mass assembly and chemical enrichment of the first galaxies provide key insights into their star-formation histories and the earliest stellar populations at cosmic dawn. Here we compile and utilize new, high-quality spectroscopic *JWST*/NIRSpec Prism observations from the *JWST* archive. In particular, we extend the wavelength coverage beyond the standard pipeline cutoff ($5.3\mu\text{m}$) up to $5.5\mu\text{m}$, which enable for the first time a detailed examination of the rest-frame optical emission-line properties for galaxies at $z \approx 10$. Crucially, the improved calibration allows us to detect $\text{H}\beta$ and the $[\text{O III}] \lambda\lambda 4959, 5007$ doublet and resolve the auroral $[\text{O III}] \lambda 4363$ line for the 11 galaxies in our sample ($z = 9.3 - 10.0$) to obtain direct T_e -based metallicity measurements. We find that the interstellar medium (ISM) of all galaxies show high ionisation fields and electron temperatures, with derived metallicities in the range $12 + \log(\text{O}/\text{H}) = 7.1 - 8.3$ (3–50% solar), consistent with previous strong-line diagnostics based on *JWST* data at high redshifts. We derive an empirical relation for M_{UV} and $12 + \log(\text{O}/\text{H})$ at $z \approx 10$, useful for future higher-redshift studies, and show that the sample galaxies are ‘typical’ star-forming galaxies though with relatively high specific star-formation rates (median $\text{sSFR} = \text{SFR}_{\text{H}\beta}/M_{\star} = 58 \text{ Gyr}^{-1}$) and with evidence for bursty star formation on 10 Myr vs 100 Myr timescales ($\log_{10}(\text{SFR}_{10}/\text{SFR}_{100}) = 0.4$). Combining the rest-frame optical line analysis and detailed UV to optical spectro-photometric modelling, we determine the mass-metallicity relation (MZR) and the fundamental-metallicity relation (FMR) of the sample, pushing the previous redshift frontier of these measurements to $z = 10$. These results, together with literature measurements, point to a gradually decreasing MZR at higher redshifts, with a break in the FMR at $z \approx 3$, decreasing to metallicities $\approx 3\times$ lower at $z = 10$ than observed in galaxies during the majority of cosmic time at $z = 0 - 3$, likely caused by massive pristine gas inflows diluting the observed metal abundances during early galaxy assembly at cosmic dawn.

Key words. high-redshift galaxies – galaxy formation, evolution

1. Introduction

Probing the chemical enrichment of the first galaxies in the early Universe is key to constrain the physical processes that regulate their formation and evolution via gas inflows and outflows, star formation, and the synthesis of heavier elements in stellar cores. This process has been characterized by the scaling relation between the stellar mass and chemical abundance of oxygen, known as the mass-metallicity relation (Lequeux et al. 1979; Tremonti et al. 2004; Lee et al. 2006; Erb et al. 2006; Kewley & Ellison 2008). Perhaps more fundamental is the additional scaling with the star-formation rate, called the fundamental-metallicity relation (Ellison et al. 2008; Mannucci et al. 2010; Lilly et al. 2013; Andrews & Martini 2013; Curti et al. 2020), which has been found to be constant out to $z \approx 3$ (Sanders et al. 2021), throughout the majority of cosmic time. This implies universal galaxy growth, potentially representing the universal scal-

ing between the molecular gas mass surface density and star formation (Baker et al. 2023).

Rest-frame optical spectroscopy of strong nebular emission lines enables key insights into the physical properties and chemical enrichment of star-forming regions in galaxies through cosmic time (see e.g., Maiolino & Mannucci 2019; Kewley et al. 2019, for reviews). With the advent of *JWST* and its suite of sensitive, near-infrared spectroscopic capabilities (Jakobsen et al. 2022), it is now possible to measure and constrain rest-frame optical nebular emission lines out to very high redshifts. The first studies of a statistical sample of galaxies at $z \approx 8$ with detected rest-frame optical emission lines (Langeroodi et al. 2023; Heintz et al. 2023a; Sanders et al. 2024) revealed a significantly decreasing metallicity at a given stellar mass compared to past measurements out to $z \approx 3$. This was later confirmed by larger *JWST* samples (Nakajima et al. 2023; Curti et al. 2024; Morishita et al. 2024), and for very low stellar mass ($M_{\star} \sim 10^6 M_{\odot}$) (Chemerynska et al. 2024) to near-solar metallicities (Rowland

et al. 2025). Perhaps most surprising was the apparent offset from the fundamental-metallicity relation towards 0.5 dex lower metallicities for a given stellar mass and star-formation rate (Heintz et al. 2023a), hinting at a transition period for high-redshift galaxies dominated by pristine gas inflows, though the exact redshift is still debated (constrained to within $z \sim 4 - 8$; Nakajima et al. 2023; Curti et al. 2024). Strong-line measurements further enable the determination of the relative elemental abundances and the ionisation fields of the interstellar medium (ISM) (e.g., Schaerer et al. 2022; Arellano-Córdova et al. 2022, 2024; Heintz et al. 2023b; Trump et al. 2023; Shapley et al. 2023a) for some of the most distant galaxies known out to $z \approx 9$.

Most of the previous metallicity measurements of high-redshift galaxies have relied on strong-line diagnostics due to the inaccessibility of the temperature-sensitive [O III] $\lambda\lambda 4363$ auroral lines, either due to its intrinsic faintness or because it is blended with H γ in low-resolution spectra. However, a growing number of direct measurements using the direct ‘ T_e -method’ are now being reported based on *JWST* grating spectra (Laseter et al. 2024; Sanders et al. 2024; Scholte et al. 2025; Cullen et al. 2025), which has been crucial to calibrate the empirical strong-line relations for the majority of galaxies with no auroral line detection. Despite the growing number of T_e -based $12+\log(\text{O}/\text{H})$ estimates, there are still relatively few at $z > 9$. Here we utilize new, custom reductions of recent *JWST*/NIRSpec Prism spectroscopic data, expanding the wavelength coverage out to $5.5\mu\text{m}$ (up from $5.3\mu\text{m}$), to investigate the rest-frame UV and optical lines up to and including the [O III] $\lambda\lambda 4959, 5007$ line doublet at $z = 10.0$. These we use to benchmark against existing high-redshift strong-line diagnostics and determine fundamental galaxy scaling relations up to the highest redshifts achievable by *JWST*/NIRSpec.

We structure the paper as follows. In Sect. 2 we present our new spectroscopic reductions of archival *JWST* data and detail the sample compilation. In Sect. 3 we describe the emission-line analyses and spectro-photometric modelling and in Sect. 4 we present the new empirical galaxy scaling relations at $z \approx 10$. In Sect. 5 and Sect. 6 we discuss and conclude on our work. Throughout the paper we assume the standard concordance cosmology, with a flat, Λ CDM-dominated Universe. We adopt the cosmological parameters from Planck Collaboration et al. (2020) and the solar abundances from Asplund et al. (2009) with $12 + \log(\text{O}/\text{H})_\odot = 8.69$.

2. Observations

For this work, we compile and utilize the archival *JWST* data reduced and processed as part of the DAWN *JWST* Archive (DJA)¹. This online repository contains reduced images, photometric catalogs, and spectroscopic data for public *JWST* data products. The raw spectroscopic data are retrieved from MAST, before they are processed with MSAExp (Brammer 2023)², as detailed in Heintz et al. (2025, for version 2, v2) and de Graaff et al. (2024, for v3), respectively.

Here we present and utilize the most recent spectra from v4 of the DJA spectroscopic archive (see also Valentino et al. 2025). We focus on the spectra observed with the *JWST*/NIRSpec Prism configuration (Jakobsen et al. 2022), which nominally covers $\lambda = 0.6 - 5.3\mu\text{m}$ with a resolving power $\mathcal{R} \approx 100$. Briefly, DJA-v4 uses updated *JWST* reference files, and includes a bar shadow correction, overall improving the absolute and colour-dependent

flux calibration. Newly, we extend the wavelengthrange reference file³ to include the 2nd and 3rd order Prism spectra, which were cut from the *JWST* pipeline to avoid the higher-order contamination on the primary first spectral order (Jakobsen et al. 2022). These, however, appear at predictable locations and intensities, and are therefore now carefully calibrated into the DJA-v4 reductions to include the full response of the telescope and thereby recover the full spectrum recorded on the detector (see also Valentino et al. 2025, for details on the same procedure on the higher-resolution grating spectra). This effectively extends the wavelength coverage of NIRSpec Prism to $5.5\mu\text{m}$. The final 1D spectra were optimally extracted (Horne 1986) and the flux calibrations are generally accurate to the photometry (see below). The v4 reductions have been run and processed on the entire DJA, including also more recent public *JWST*/NIRSpec observations, and can be found on the dedicated online repository⁴.

Consequently, we can now detect and constrain the rest-frame optical emission lines such as the crucial [O III] $\lambda\lambda 4959, 5007$ doublet up to $z = 10.0$ with *JWST*/NIRSpec (instead of only up to $z \approx 9.5$ with standard pipeline products). Due to increasing spectral resolution with wavelength, and the generally higher delivered resolving power, we measure up to $\mathcal{R} \approx 500$ at $5.5\mu\text{m}$. This increased resolution is sufficient to spectroscopically resolve the [O III] $\lambda\lambda 4363$ auroral line transition from H γ at $z \gtrsim 9.0$, allowing direct, T_e -based metallicity estimates at $z = 9.0 - 10.0$. We compile a set of 11 galaxies from DJA-v4 with *JWST*/NIRSpec Prism spectra, by requiring a robust detection of H β ($\text{S/N} > 5$) and wavelength coverage of the [O III] $\lambda\lambda 4959, 5007$ doublet. This mainly includes galaxies observed as part of the major *JWST* spectroscopic surveys: CAPERS (prog. ID: 6368, PI: Dickinson; Kokorev et al. 2025), JADES (prog. IDs: 1181 and 3215, PI: Eisenstein; Bunker et al. 2023; Eisenstein et al. 2023a,b), UNCOVER (prog. ID: 2561, PIs: Labbe and Bezanson; Bezanson et al. 2022), RUBIES (prog. ID: 4233, PIs: de Graaff & Brammer; de Graaff et al. 2024) and RXJ DDT (prog. ID: 2767, PI: Kelly). The final sample is summarized in Table 1.

For each galaxy, the photometric data obtained primarily with *JWST*/NIRCam through DJA (Valentino et al. 2023) was inspected, in order to photometrically calibrate the flux density of the spectra. Of the 11 galaxies in the sample, only two require a positive (>1) scaling, consistent with slit loss. For these objects the spectra were calibrated using BAGPIPES during the spectro-photometric modelling of the spectral energy distribution (SED), and the calibrated spectra were used for line-fitting. For the remainder of the sample, the photometry is either consistent with spectroscopy; not requiring rescaling, or lower than the spectrum for no obvious physical reason from inspecting the morphology. The analysis for these galaxies is carried out directly on the DJA-reduced spectra.

3. Analysis and results

3.1. Emission-line modelling

We model the most prominent rest-frame optical nebular emission lines detected in the spectra, from the (unresolved) [O II] $\lambda\lambda 3726, 3729$ doublet to the [O III] $\lambda\lambda 4959, 5007$ doublet line transitions. Due to the expanded wavelength coverage, the

¹ <https://dawn-cph.github.io/dja/>

² github.com/gbrammer/msaexp

³ https://jwst-pipeline.readthedocs.io/en/latest/jwst/references_general/wavelengthrange_reffile.html

⁴ https://s3.amazonaws.com/msaexp-nirspec/extractions/public_prelim_v4.2.html

Table 1. Sample overview with derived redshifts and rest-frame optical emission-line fluxes, or 3σ upper limits.

Source	z_{spec}	[O II] $\lambda\lambda 3726, 29$	[Ne III] 3869	H γ	[O III] $\lambda 4363$	H β	[O III] $\lambda 5007$
CAPERS-EGS-25297	9.9381 ± 0.0003	$73.0^{+3.3}_{-3.3}$	$71.8^{+3.1}_{-3.1}$	$75.7^{+4.1}_{-4.0}$	$28.2^{+3.8}_{-3.8}$	$207.2^{+6.9}_{-6.8}$	$1172.6^{+9.5}_{-9.7}$
UNCOVER-2561-13151 ^(a*)	9.8026 ± 0.0003	$7.0^{+2.2}_{-2.2}$	$22.6^{+2.3}_{-2.3}$	$15.5^{+2.5}_{-2.6}$	< 7.7	$52.7^{+3.6}_{-3.5}$	$288.4^{+7.9}_{-7.6}$
JADES-GN-55757	9.7498 ± 0.0006	$16.7^{+4.4}_{-4.5}$	$18.1^{+4.9}_{-4.9}$	$47.9^{+5.3}_{-5.3}$	< 15.8	$72.2^{+6.9}_{-6.9}$	$339.4^{+12.0}_{-11.6}$
UNCOVER-2561-22223 ^(b*)	9.5704 ± 0.0008	< 10.04	$10.3^{+3.4}_{-3.3}$	$22.9^{+4.1}_{-4.0}$	< 12.6	$74.7^{+5.7}_{-5.9}$	$229.7^{+7.5}_{-7.6}$
RXJ2129-2767-11027 ^(c*)	9.5127 ± 0.0001	$1.9^{+0.4}_{-0.4}$	$2.1^{+0.4}_{-0.4}$	$4.2^{+0.5}_{-0.4}$	$1.9^{+0.5}_{-0.5}$	$7.3^{+0.6}_{-0.6}$	$40.5^{+0.8}_{-0.7}$
JADES-GS-265801 ^(d)	9.4437 ± 0.0001	$9.4^{+0.9}_{-0.8}$	$27.0^{+1.0}_{-0.9}$	$34.5^{+1.0}_{-1.0}$	$14.1^{+1.0}_{-1.0}$	$81.5^{+1.3}_{-1.3}$	$480.3^{+2.0}_{-2.0}$
CAPERS-EGS-87132	9.3833 ± 0.0002	$17.6^{+2.9}_{-2.9}$	$25.3^{+3.1}_{-3.1}$	$20.6^{+3.6}_{-3.6}$	$12.3^{+3.4}_{-3.4}$	$38.4^{+4.0}_{-4.1}$	$282.8^{+5.7}_{-5.5}$
JADES-GN-3990	9.3812 ± 0.0002	$16.6^{+2.6}_{-2.5}$	$22.2^{+2.5}_{-2.5}$	$25.4^{+3.0}_{-3.0}$	$12.3^{+2.7}_{-2.9}$	$54.6^{+3.6}_{-3.6}$	$366.4^{+4.7}_{-4.8}$
UNCOVER-2561-3686 ^(e*)	9.3202 ± 0.0004	$73.6^{+10.5}_{-10.5}$	$79.1^{+10.7}_{-10.5}$	$48.4^{+10.4}_{-10.5}$	< 32.9	$49.2^{+12.5}_{-12.5}$	$639.5^{+16.0}_{-15.5}$
RUBIES-UDS-833482	9.3042 ± 0.0003	$93.1^{+13.9}_{-13.9}$	$70.3^{+12.7}_{-12.9}$	$91.9^{+15.9}_{-15.3}$	< 36.2	$165.7^{+16.0}_{-15.7}$	$1595.2^{+26.2}_{-26.2}$
CAPERS-UDS-22431	9.2717 ± 0.0001	$27.1^{+3.1}_{-3.2}$	$44.5^{+3.4}_{-3.5}$	$35.8^{+3.7}_{-3.8}$	$19.8^{+3.7}_{-3.7}$	$88.2^{+4.7}_{-4.7}$	$727.8^{+6.9}_{-6.9}$

Notes. Selected galaxies have reported/analysed in previous works: ^(a) Zitrin et al. (2014); Roberts-Borsani et al. (2023); Fujimoto et al. (2023) ^(b) Fujimoto et al. (2023) ^(c) Williams et al. (2023) ^(d) Curti et al. (2025) ^(e) Boyett et al. (2024); Atek et al. (2023); Castellano et al. (2023); Fujimoto et al. (2023). ^(*) Lensed galaxies, the reported line fluxes are not corrected for magnification.

The [O II] $\lambda\lambda 3726, 3729$ line doublet is blended so we report the total line fluxes. We use the theoretical ratio of [O III] $\lambda 5007$ /[O III] $\lambda 4363 \sim 2.98$ to fix the line flux of [O III] $\lambda 4363$. All line fluxes are uncorrected for dust attenuation and in units of $10^{-20} \text{ erg s}^{-1} \text{ cm}^{-2}$.

latter can now be measured up to $z = 10.0$, while simultaneously resolving the auroral [O III] $\lambda 4363$ line from H γ . We determine the line fluxes or upper bounds on the emission lines by modelling the full set of lines jointly with Gaussian line profiles (at vacuum wavelengths), tying the redshift and intrinsic width (convolved with the Prism spectral resolution). We model the underlying continuum with a simple first-order polynomial. To estimate the model parameters, we use Dynamic Nested Sampling from DYNESTY (Speagle 2020), which allows for more complex distributions to be modelled (Koposov et al. 2022; Higson et al. 2019).

An example of the line fitting, highlighting the spectroscopically resolved [O III] $\lambda 4363$ line, is shown in Fig. 1. We find that the observed spectral resolution is typically 1.20–1.70 higher than the nominal *JWST*/NIRSpec Prism curve at any given wavelength (see also e.g., de Graaff et al. 2024). The derived line fluxes and derived redshifts are summarized in Table 1. The observed line fluxes were corrected for dust-reddening using SED-derived extinction A_V values, from the BAGPIPES fits outlined in Sect. 3.3. Emission line fluxes are corrected assuming a modified Calzetti et al. (2000) dust curve (see Salim et al. (2018); Salim & Narayanan (2020)), with slope $\delta = -0.3$ and $R_V = 3.0$. We find the sample is generally dust-poor, with a maximum $A_V = 0.36$, and mean $A_V \sim 0.2$. The dust-corrected line fluxes are used for emission line ratios, as well as for derivations of T_e , $12 + \log(\text{O}/\text{H})$, and $\text{SFR}(\text{H}\beta)$.

Figure 2 shows the main line ratios of the strongest nebular lines, highlighting the typical ionisation fields, electron temperatures and diagnostics to separate active galactic nuclei (AGN) vs. star-forming galaxies. Here we also compare to the low-redshift ($z < 0.3$) galaxy sample from the Sloan Digital Sky Survey (SDSS; Aihara et al. 2011), for reference. The SDSS line fluxes were corrected for dust attenuation using the Balmer decrement, assuming $\text{H}\alpha/\text{H}\beta = 2.86$ (Case B, $T_e = 10,000\text{K}$), and a Calzetti et al. (2000) dust curve.

Strong nebular line ratios have typically been used to distinguish the intrinsic emission from AGN or star-forming regions. The classic Baldwin-Phillips-Terlevich (BPT) diagram (Baldwin et al. 1981) separating the dominant emission com-

ponents is based on the [O III] $\lambda 5007/\text{H}\beta$ vs. [N II] $\lambda 6584/\text{H}\alpha$ line ratios. However, this is obfuscated at high redshifts due to the general increased intensity of the ISM ionisation fields (Calabrò et al. 2024; Roberts-Borsani et al. 2024), and we are unable to measure [N II] $\lambda 6584/\text{H}\alpha$ with NIRSpec beyond $z \approx 8.3$. New classification diagnostics have therefore been developed, focusing on particularly the O3Hg = $\log_{10}([\text{O III}] \lambda 4363/\text{H}\gamma)$ line ratio (Mazzolari et al. 2024; Backhaus et al. 2025). In Panels (a)-(b) of Fig. 2, we show the O3Hg line ratios compared to O32 = $\log_{10}([\text{O III}] \lambda 5007/[\text{O II}] \lambda 3727)$ and O33 = $\log_{10}([\text{O III}] \lambda 5007/[\text{O III}] \lambda 4363)$, representing the ionisation field and T_e , respectively. We note that the O3Hg line ratios are only slightly higher than the low-redshift reference sample, likely due to a combination of higher T_e but lower metallicities. While the majority of our sample are located in the star-forming locus for panels (a)-(b), they lie close to the boundary, and many are situated in the AGN region (albeit also along the boundary) for panel (c), where O3Hg is plotted with $\text{Ne3O2} = \log_{10}([\text{Ne III}] \lambda 3869/[\text{O II}] \lambda 3727)$. Given the difficulty of distinguishing star-forming galaxies and AGN at high- z , and relying on faint emission lines for the diagnostics, we cannot rule out the presence of AGN in the sample. If present, the contribution could affect metallicity and stellar mass measurements. However, since the sample lies along the boundary, and there is no overwhelming evidence to suggest AGN are present, we assume these are star-forming sources in the following analysis.

In Panel (d), we show O32 relative to the O33, the latter inversely correlating the electron temperature T_e of the H II region. We find no clear correlation between the lines ratios for the galaxies at $z = 9 - 10$ but highlight the typical lower [O III] $\lambda 5007/[\text{O III}] \lambda 4363$ ratios at high- z , indicating higher T_e in the ISM of these galaxies. In Panel (e), we show the Ne3O2 vs the O32 line ratios, which are both sensitive to the same ionisation field since [Ne III] and [O III] originate in the same high-ionisation zone of the H II region (with ionisation potentials greater than ~ 40 and 35 eV). We find that both these line ratios are substantially higher than for the typical low-redshift galaxy population, as also found previously for *JWST*-observed galaxies up to $z \sim 8$ (Schaerer et al. 2022; Curti et al. 2023; Roberts-

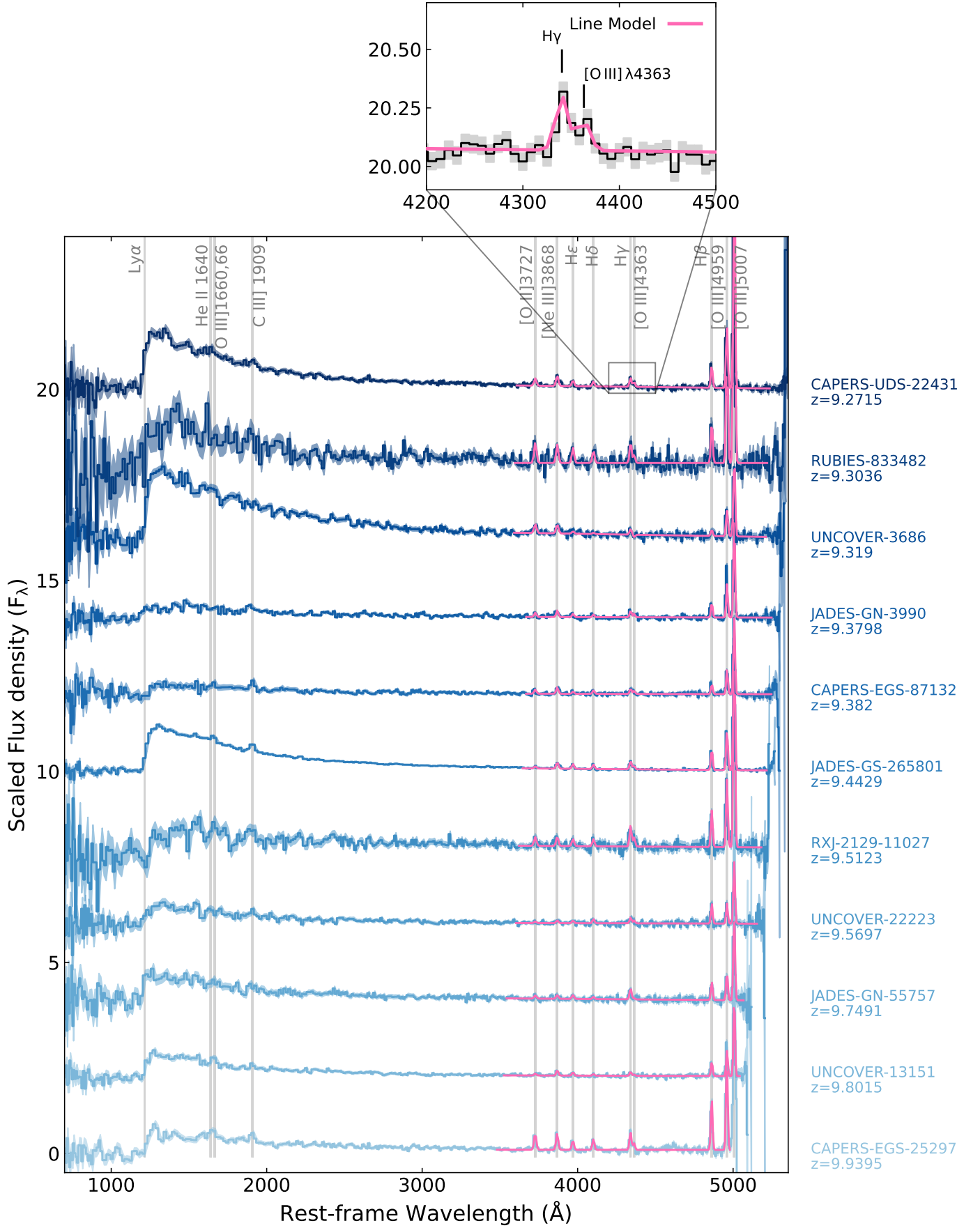


Fig. 1. *JWST*/NIRSpec Prism 1D spectroscopy of the sample, shown in shades of blue, with the associated error spectrum as a shaded region. The position of the main line transitions are highlighted by grey lines. The inset zooms in on the spectroscopically resolved H γ + [O III] λ 4363 emission lines, with the best-fit continuum and emission-line model for each galaxy shown by the pink lines.

Borsani et al. 2024). This indicates a higher ionisation parameter in these early systems, with median $\log U \approx -2$, quantified from diagnostics based on O32 and Ne3O2 (Díaz et al. 2000; Witstok et al. 2021).

3.2. Direct T_e -based metallicities

We determine the metallicities using the direct ‘ T_e -based’ method (Peimbert et al. 2017; Pérez-Montero 2017; Kewley et al. 2019; Osterbrock & Ferland 2006) which relies on measuring the electron temperature T_e to determine gas-phase metallicity $12+\log(\text{O}/\text{H})$. This assumes low electron densities ($n_e \lesssim 10^5 \text{ cm}^{-3}$), which appear common for galaxies at $z \sim 10$ (Hsiao et al. 2024a; Isobe et al. 2023; Topping et al. 2025).

We estimate electron temperature T_e with the $[\text{O III}]\lambda 4363/[\text{O III}]\lambda 5007$ ratio, using the `getTemDen` routine in `PyNEB` (Luridiana et al. 2015). As the $[\text{O II}]$ doublet is unresolved we do not have a direct constrain on electron density. However, $n_e = 300 \text{ cm}^{-3}$ is typical of star-forming galaxies at $z \sim 2.3$ (Sanders et al. 2016); although *JWST* results have shown that there is likely to be a trend of increasing electron density with redshift (Topping et al. 2025; Abdurro’uf et al. 2024; Li et al. 2025a; Isobe et al. 2023; Harikane et al. 2025). While we fiducially assume an electron density of $n_e = 300 \text{ cm}^{-3}$, we find changing the density up to $n_e \sim 1 \times 10^4 \text{ cm}^{-3}$ has at most 0.02 dex impact on the abundance measurements. Harikane et al. (2025) have suggested a more accurate method would be combining *JWST* and *ALMA* observations and using a 2-zone ISM model to trace both high and low-density regions, as assuming a constant density and temperature throughout the ISM may result in underestimating the oxygen abundance by up to 0.8 dex.

As determining singly-ionised oxygen abundance O^+ requires a temperature that traces the low-ionisation zone of the gas, we assume a relation between temperatures of the high and low ionisation zones $T_e([\text{O II}]) = 0.7 \times T_e([\text{O III}]) + 3000 \text{ K}$ from Garnett (1992). Cataldi et al. (2025) suggest a new $T_3 - T_2$ relation for $z \sim 2 - 3$, although using this calibration changes the oxygen abundance of the sample on average 0.01 dex, as the galaxies are highly ionised so the O^+ abundance is generally low. The total oxygen abundance is then calculated by summing the contributions from different ionic abundances $\text{O}/\text{H}^+ = \text{O}^+/\text{H}^+ + \text{O}^{++}/\text{H}^+$ obtained with `getIonAbundance`. The contribution from O^{+++} is not included as it is likely to be negligible even under the most extreme ISM conditions (Cullen et al. 2025; Berg et al. 2021). The errors on all gas-phase properties are obtained using 1000 Monte Carlo simulations, where line fluxes are perturbed randomly according to their measured uncertainties. We employ the transition probabilities and collisional strengths included in `PyNEB`; all atomic data from Froese Fischer & Tachiev (2004), collisional data from Kisieliński et al. (2009) for O^+ , and Aggarwal & Keenan (1999) for O^{++} .

The determine direct metallicities (and 3σ upper limits) for the full sample are listed in Table 2 and shown in Fig. 3, ranging from $12+\log(\text{O}/\text{H}) \approx 7.1 - 8.3$. We compare to high- z literature diagnostics from Sanders et al. (2024), Laseter et al. (2024), Scholte et al. (2025), and high equivalent width (EW) low- z diagnostics from Nakajima et al. (2022). Our sample are generally in good agreement with these calibrations, (with considerable scatter, as was also seen in previous works) though we do not have a large enough statistical sample to distinguish between those that diverge. Our derived metallicities for RXJ2129-11767-11027 and JADES-GS-265801 are consistent within ~ 0.1 dex to the values reported in previous literature;

respectively $12+\log(\text{O}/\text{H}) = 7.48 \pm 0.08$ (Williams et al. 2023, from strong-line ratios) and 7.49 ± 0.11 (Curti et al. 2025, using the direct method, with ionisation correction factors).

3.3. Spectro-photometric SED modelling

To derive the stellar continuum properties of our sample, in particular the stellar masses, we perform spectro-photometric modelling of the spectral energy distribution (SED) of each source based on the *JWST*/NIRSpec PRISM spectroscopy and available broad-band NIRCам photometry. We summarise our modelling methods below.

In order to estimate the SED model posteriors, we use the code Bayesian Analysis of Galaxies for Physical Inference and Parameter ESTimation (BAGPIPES, Carnall et al. 2018, 2019) which performs nested-sampling using the NAUTILUS (Lange 2023) algorithm. Within BAGPIPES, we use the Binary Population and Spectral Synthesis code (BPASS) v2.2.1⁵ stellar population synthesis (SPS) models (Stanway & Eldridge 2018) to build galaxy SEDs based on a broken power-law initial mass function (IMF), where the slope of the power law is $\alpha_1 = -1.30$ for $M_\star \in (0.1, 0.5) M_\odot$ and $\alpha_2 = -2.35$ for $M_\star \in (0.5, 300) M_\odot$. We use nebular line and continuum emission models from the CLOUDY photoionisation code (Ferland et al. 2017; Byler et al. 2017), where the CLOUDY grids are calculated using the BPASS SPS models as the input ionising source.

To account for slit losses, the *JWST*/NIRSpec PRISM spectra are flux-calibrated to the NIRCам broadband photometry self-consistently within the BAGPIPES framework with a second-order Chebyshev polynomial. Gaussian priors are set on the polynomial coefficients by performing an initial least-squares fit to the ratio between the observed photometry to the synthetic photometry (calculated by integrating the NIRSpec spectrum through the NIRCам filter profiles⁶). From an initial SED modelling run, we find that only two sources in our sample require photometric scaling, JADES-GN-3990 and UNCOVER-2561-3686; for the rest, we perform SED modelling without the calibration described above.

We model the SEDs with a non-parametric continuity star-formation history (SFH; Leja et al. 2019), which allows for flexible star-formation rates (SFRs) in a sequence of user-defined time steps. The initial few time step edges are fixed in lookback time at $[0, 10, 50, 100]$ Myr, after which the timesteps are equally space in logarithmic lookback time between 100 Myr and the age on the universe at $z = 30$. The number of time steps therefore is redshift-dependent. We impose a Student’s t distribution on the change in the SFR between adjacent time bins, with the distribution being centred at 0 with a scale factor $\sigma = 0.3$ and $\nu = 2$ (Leja et al. 2019). We set a logarithmic prior on the formed stellar mass, $M_{\text{formed}}/M_\odot \in (10^6, 10^{14})$. We set a Gaussian prior on the metallicity, centred on the direct T_e -based measurements derived in Sect. 3.2 with a scatter of 10% Z_\odot . For galaxies with only a lower limit on T_e -based metallicities, strong-line diagnostics were instead used to quantify the oxygen abundance (see Eq. 1; Sect. 4.3).

The dust is modelled with a Salim et al. (2018) dust curve, where we fix the slope of the attenuation curve to $\delta = -0.3$ and the strength of the 2175Å UV bump is fit in the range $B \in (0, 3)$ with a uniform prior. An extra factor of attenuation is applied to starlight within stellar birth clouds, where $\eta = 2$. We adopt a uniform prior on the V -band attenuation, where $A_V \in (0, 1)$ mag.

⁵ <https://bpass.auckland.ac.nz/9.html>

⁶ <https://svo2.cab.inta-csic.es/theory/fps/>

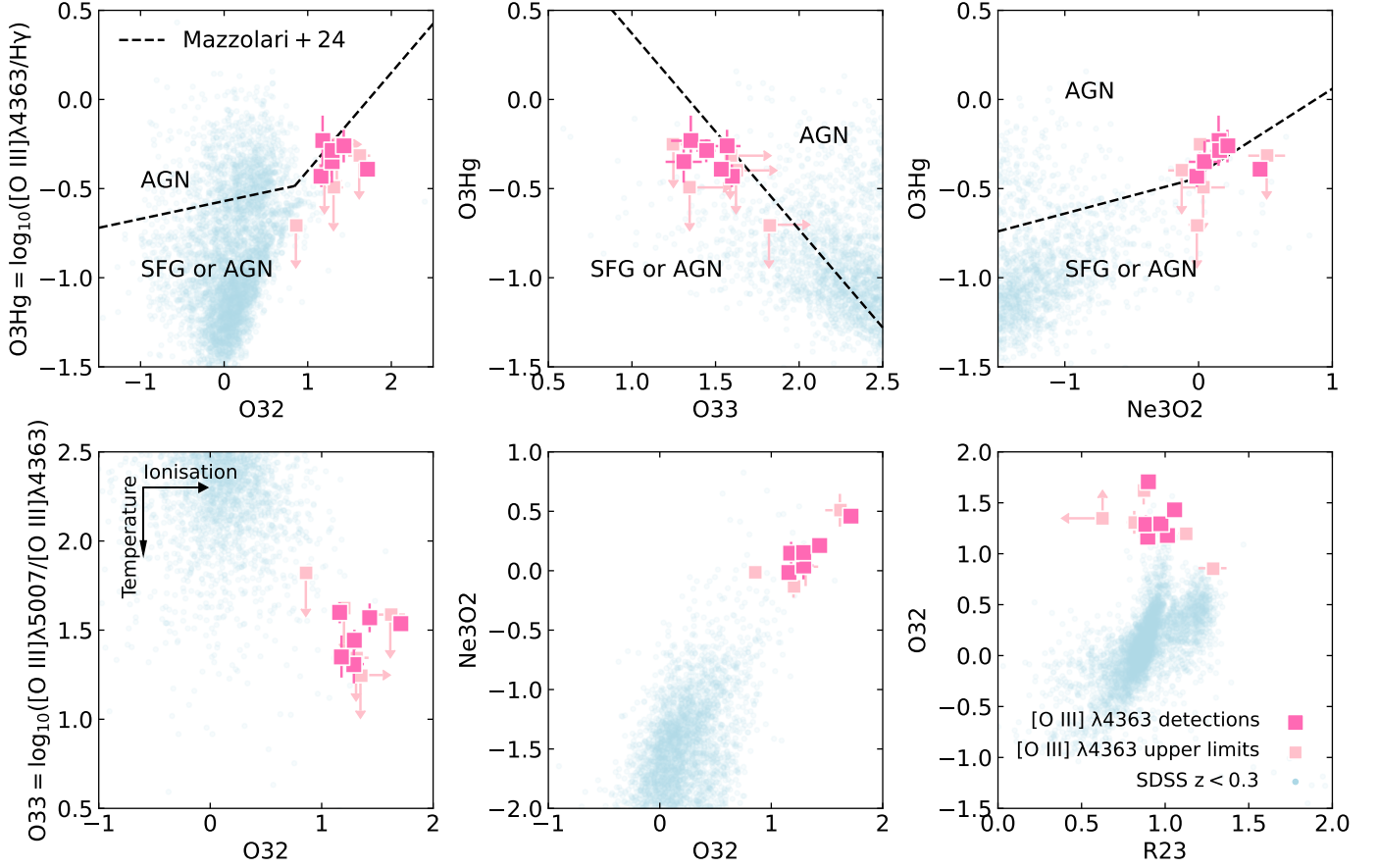


Fig. 2. Line flux ratios of the $z = 9$ sample, with $[\text{O III}]\lambda 4363$ detections in hot pink, and 3σ upper limits in pale pink. The blue points show $z \approx 0$ galaxies with $[\text{O III}]\lambda 4363$ detections from SDSS-DR15, for comparison. The dashed lines represent AGN diagnostics utilising the $[\text{O III}]\lambda 4363$ auroral line from Mazzolari et al. (2024), calibrated using local and high- z samples of SFGs and AGN.

The nebular ionisation parameter is varied in the range $\log U \in (-4, -1)$ with a uniform prior. We set a tight Gaussian prior on the redshift centered at the spectroscopic redshift derived from MSAEXP on the DJA, with $\sigma_z = 0.001 \times (1 + z_{\text{spec}})$. The velocity dispersion is fixed to 100 km/s. A logarithmic prior is set on the white noise scaling in the range (1., 10.).

We caution that the posterior parameter estimates from the SED modelling are heavily model-dependent, where in particular the stellar mass may be subject to ‘outshining effects’ (e.g., Giménez-Arteaga et al. 2023; Narayanan et al. 2024), and the assumed SFH and IMF (e.g., Carnall et al. 2018; Leja et al. 2019; Steinhardt et al. 2023; Straat et al. 2023).

4. Galaxy properties at $z \approx 10$

4.1. Rest-frame UV properties

The derived galaxy properties are summarized in Table 2. We first consider the direct, measured properties of the targeted galaxies at $z = 9 - 10$. For the absolute rest-frame UV magnitude, we integrate the flux density of the spectrum with a 100Å top-hat filter centred at rest-frame 1500 Å. We fit a standard power-law slope, assuming $F_{\lambda, \text{obs}} \propto \lambda^{-\beta_{\text{UV}}}$ to determine β_{UV} , carefully masking the most prominent nebular emission lines in the modelling. The large scatter, from $\beta_{\text{UV}} = -1.5$ to -2.8 and $M_{\text{UV}} = -16$ to -21 mag are consistent with larger samples using photometric (Topping et al. 2024; Cullen et al. 2024; Austin et al. 2024) and spectroscopic (Saxena et al. 2024; Dottorini et al.

2024) measurements. We do not observe any strong correlations between M_{UV} and β_{UV} in our spectroscopic sample at $z = 9 - 10$, where typically brighter, more massive galaxies would be expected to show redder rest-frame UV slopes.

In Figure 4.1, we compare M_{UV} to the oxygen abundance $12 + \log(\text{O}/\text{H})$. For comparison to our sample we plot the lensed galaxy MACS0647-JD1 at $z = 10.17$ (Hsiao et al. 2023), as the only other galaxy with a direct metallicity determination at $z \sim 10$. We find a clear correlation between M_{UV} and direct $12 + \log(\text{O}/\text{H})$ (including MACS0647-JD1, but not lower limits), with a best-fit relation of $M_{\text{UV}} = (-8.55 \pm 1.98)Z + (46.4 \pm 15.1)$, with $Z = 12 + \log(\text{O}/\text{H})$. This is expected given that the most massive, star-forming galaxies are likely also to show higher metal enrichment at a given SFR. This strong correlation (with a Spearman correlation coefficient $\rho = -0.94$, Pearson coefficient $r = -0.91$) further provides a viable relation to infer the gas-phase metallicities for galaxies at $z \gtrsim 10$ with only measures of M_{UV} . We do not recover any apparent trend relating β_{UV} to $12 + \log(\text{O}/\text{H})$, where increased dust reddening would be expected to scale with the metallicity. This indicates that the rest-frame UV slope is likely not representing the overall dust content of high-redshift galaxies, potentially due to more dominating nebular continua at low metallicities (Cameron et al. 2024; Katz et al. 2024).

⁷ <https://jwst-uncover.github.io>

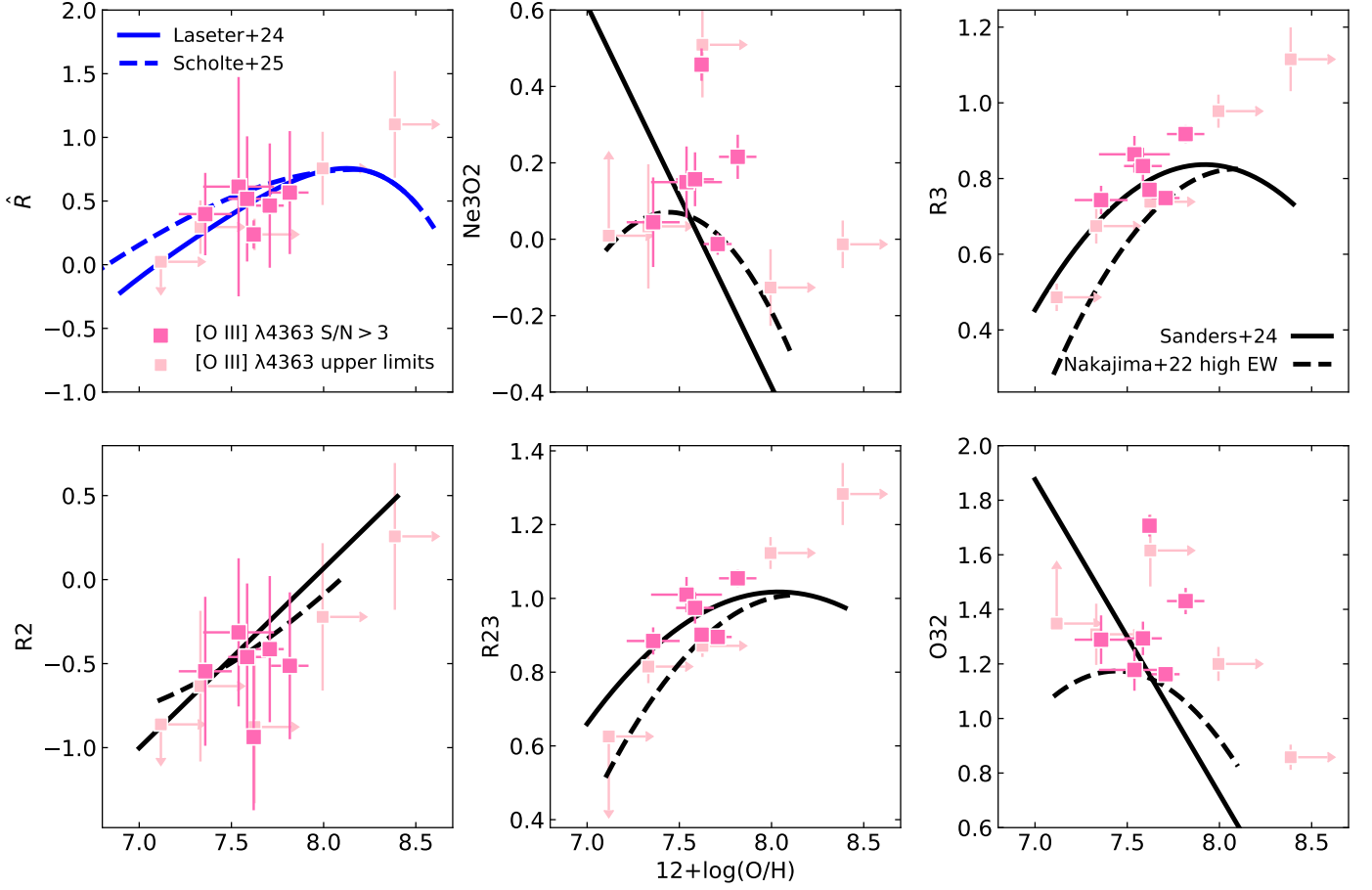


Fig. 3. T_e -based metallicities and strong-line ratios for the $z > 9$ sample. Direct oxygen abundances are represented by hot pink square markers, with 3σ upper limits in pale pink. We compare to various literature strong-line diagnostics: the solid and dashed blue relations shows Laseter et al. (2024) and Scholte et al. (2025) \hat{R} calibrations, solid and dashed black curves are Ne3O2, R3, R2, R23, O32 diagnostics from Sanders et al. (2024) and Nakajima et al. (2022) respectively.

Table 2. Summary of the main galaxy properties for our $z > 9$ sample, including UV magnitude M_{UV} , UV continuum slope β_{UV} , stellar mass, star-formation rates derived from H β , electron temperature T_e , and direct T_e based metallicities derived using PYNEB.

Source	M_{UV}/mag	β_{UV}	$\log_{10}(M_{\star}/M_{\odot})$	$\log_{10}(\text{SFR}_{H\beta}/M_{\odot} \text{ yr}^{-1})$	$12+\log(\text{O}/\text{H})$	$T_e/10^4\text{K}$
CAPERS-EGS-25297	-19.47 ± 0.26	-1.48 ± 0.05	$8.39^{+0.04}_{-0.02}$	1.32 ± 0.02	7.69 ± 0.08	1.7 ± 0.12
UNCOVER-2561-13151 (*)	-16.29 ± 0.27	-2.45 ± 0.06	$6.97^{+0.10}_{-0.10}$	-0.48 ± 0.03	> 7.65	< 1.71
JADES-GN-55757	-19.19 ± 0.51	-2.34 ± 0.09	$8.05^{+0.16}_{-0.17}$	0.74 ± 0.04	> 7.35	< 2.41
UNCOVER-2561-22223 (*)	-17.15 ± 0.55	-2.60 ± 0.19	$6.99^{+0.15}_{-0.05}$	0.10 ± 0.03	> 7.11	< 2.91
RXJ2129-2767-11027 (*)	-15.86 ± 0.75	-1.43 ± 0.19	$6.87^{+0.04}_{-0.03}$	-0.19 ± 0.04	7.36 ± 0.14	2.58 ± 0.52
JADES-GS-265801	-19.68 ± 0.07	-2.50 ± 0.01	$8.30^{+0.03}_{-0.03}$	0.75 ± 0.01	7.61 ± 0.04	1.83 ± 0.07
CAPERS-EGS-87132	-18.45 ± 0.63	-1.83 ± 0.13	$8.19^{+0.13}_{-0.15}$	0.48 ± 0.05	7.53 ± 0.17	2.39 ± 0.49
JADES-GN-3990	-18.65 ± 0.39	-1.30 ± 0.04	$8.59^{+0.18}_{-0.12}$	1.23 ± 0.04	7.57 ± 0.11	2.09 ± 0.18
UNCOVER-2561-3686 (*)	-20.56 ± 0.18	-2.08 ± 0.03	$9.41^{+0.01}_{-0.02}$	0.50 ± 0.08	> 8.34	< 1.35
RUBIES-UDS-833482	-19.69 ± 0.84	-2.24 ± 0.14	$8.39^{+0.03}_{-0.02}$	1.14 ± 0.04	> 7.94	< 1.66
CAPERS-UDS-22431	-19.76 ± 0.22	-2.58 ± 0.04	$8.30^{+0.04}_{-0.04}$	0.77 ± 0.02	7.81 ± 0.11	1.76 ± 0.18

Notes. (*) Lensed galaxies, with reported properties corrected for magnification with magnification factors for RXJ2129-2767-11027 obtained from Williams et al. (2023), and for UNCOVER galaxies from the lensing magnification online catalogue⁷ (Price et al. 2025; Bezanson et al. 2024; Furtak et al. 2023).

4.2. Star-formation rates and timescales

The relationship between the star-formation rate (SFR) and stellar mass, M_{\star} , also known as the star-forming galaxy main sequence (SFMS), is tightly connected for star-forming galaxies, though varying in normalization across redshifts (e.g., Brinch-

mann et al. 2004; Daddi et al. 2007; Whitaker et al. 2012; Speagle et al. 2014; Lee et al. 2015; Thorne et al. 2021). This indicates an evolving specific SFR (sSFR = SFR/ M_{\star}), with galaxies at higher redshifts being more actively forming stars at a given stellar mass (e.g., Topping et al. 2022). To investigate this relation at $z \approx 10$, we here adopt M_{\star} inferred from the non-

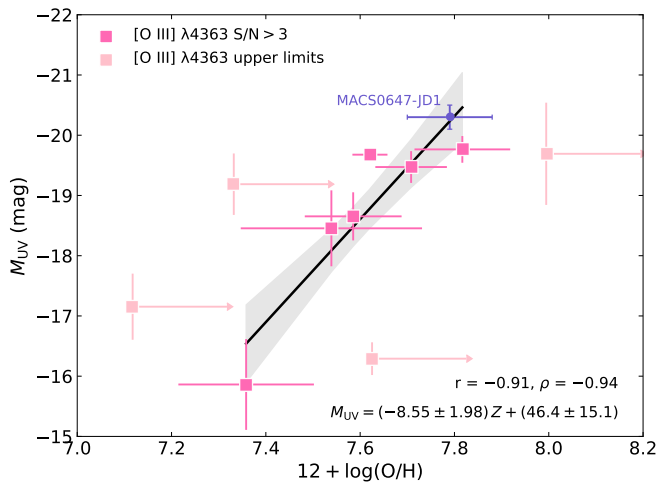


Fig. 4. UV magnitude M_{UV} versus direct T_e -based metallicity $12 + \log(\text{O}/\text{H})$. Also shown is the direct metallicity measurement of MACS0647-JD1 at $z = 10.17$ from Hsiao et al. (2023). We fit an empirical relation to the measurements (including MACS0647-JD1, but not the 3σ upper limits), shown in solid black with 1σ errors represented by the grey shaded region. The best-fit relation is reported in the bottom-right with $Z = 12 + \log(\text{O}/\text{H})$, with the associated Spearman and Pearson correlation coefficients, ρ and r , indicating a strong correlation; the most massive, UV-bright galaxies are more metal enriched.

parametric SFH model outlined in Sect. 3.3 and derive the SFR based on the $\text{H}\beta$ Balmer line luminosity. This uniquely traces the on-going star formation on relatively short, ~ 10 Myr timescales, compared to standard UV- or SED-based estimates which trace SFRs over ~ 100 Myr. We use the prescription from Shapley et al. (2023b) to determine $\text{SFR}_{\text{H}\beta}$ based on $\text{H}\alpha$, assuming a constant ratio of $\text{H}\alpha/\text{H}\beta = 2.76$ dictated from the Case B recombination scenario at $T_e = 2 \times 10^4$ K (Osterbrock & Ferland 2006) and the average metallicity for our sample of $\approx 10\%$ Solar.

In Figure 5, we show the $\text{SFR}_{\text{H}\beta} - M_\star$ relation for the galaxies at $z = 9 - 10$, compared to the full *JWST*-PRIMAL sample at $z = 3 - 9$ (Heintz et al. 2025) and other recent literature measurements at $z \gtrsim 6$ (Heintz et al. 2023a; Shapley et al. 2023b). While the sample clearly show elevated SFRs at a given mass compared to more local estimates for galaxies at $z = 0 - 4$ (e.g. Thorne et al. 2021), the SFMS is overall consistent in normalization and slope as the other literature measurements at $z \gtrsim 6$, potentially with a mild increase in SFR of 0.15 dex on average. This indicates only a marginal evolution in the SFMS from ≈ 1 Gyr to 500 Myr, consistent with the overall observed trend with redshift. The median sSFR is 58 Gyr^{-1} , $3 - 8\times$ the average value found for massive, UV bright galaxies at $z = 6 - 8$ (Topping et al. 2022). These results suggest that SFMS is already in place at $z \approx 10$, just 470 Myr after the Big Bang, and that our sample is generally comprised of ‘typical’, but very active star-forming galaxies during this epoch.

We now investigate the SFR timescales for the sample galaxies at $z \approx 10$, searching for potential signs of short-lived bursts of star formation, which might be related to the observed overabundance of UV bright galaxies at $z \gtrsim 10$ (e.g., Sun et al. 2023; Gelli et al. 2024). We compare the SFRs derived from $\text{H}\beta$ and the best-fit SED for the full galaxy sample at $z = 9 - 10$. We find that, on average, the SFR on 10 Myr to 100 Myr timescale is $\log_{10}(\text{SFR}_{10}/\text{SFR}_{100}) = 0.4$, which is $\gtrsim 2\times$ higher than the average value found at $z \approx 6$ (Endsley et al. 2024; Cole et al. 2025), but consistent with individual galaxy studies at $z \gtrsim 10$ (Kokorev

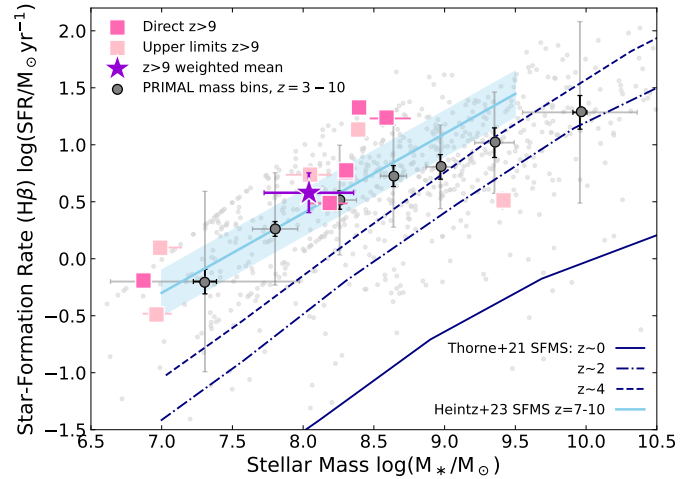


Fig. 5. The star-forming galaxy SFR – M_\star main-sequence, the $z > 9$ galaxies are plotted in pink, with the weighted mean of the sample represented by the purple star. To compare, we plot the PRIMAL sample at $z = 3 - 10$ as grey points, with the median of stellar mass bins indicated by grey markers. The solid black error bars on these markers represent the error on the median, with grey error bars showing the standard deviation of the bin. We also plot the linear relation (and empirical scatter) of the best-fit SFMS for $z = 7 - 10$ from Heintz et al. (2023a) in light blue, with dark blue curves showing the evolution of the best-fit main sequence for $z \sim 0, 2, 4$ from Thorne et al. (2021).

et al. 2025). These measurements thus provide strong evidence for highly stochastic or more bursty star formation in the general population of star-forming galaxies at $z \gtrsim 10$.

4.3. Mass-metallicity relation at $z \approx 10$

We then consider the mass-metallicity relation (MZR) for our sample in Fig. 6, extending previous analyses with *JWST* out to $z > 9$. The scaling relation between stellar mass and gas-phase metallicity is among the most studied galaxy relationships, with a relatively small intrinsic scatter (~ 0.1 dex) and strong correlation, showing more massive systems become more metal-enriched. The shape of the local MZR shows a steeper slope at low masses, which flattens at higher masses, with a turnover $\sim 10^{10} M_\odot$ (see e.g. Maiolino & Mannucci 2019, for a review). Previously, detections of $[\text{O III}] \lambda 4363$ at $z > 3$ were mostly inaccessible, but thanks to the sensitivity and wavelength coverage of NIRSpec, and the increased sample size of direct metallicity measurements, early *JWST* studies of the MZR suggest the relationship is already in place at $z = 6 - 8$ (e.g., Curti et al. 2024; Nakajima et al. 2023). We compare our direct T_e measurements and lower limits to various high- z MZR relations from literature, which use both the direct T_e method (Curti et al. 2024; Nakajima et al. 2023; Morishita et al. 2024) and strong-line calibrations (Heintz et al. 2023a). As expected, our sample galaxies are similarly less enriched for a given stellar mass than local galaxies (e.g., Curti et al. 2020); between $\sim 0.5 - 1.0$ dex.

As a benchmark, we also include additional high- z galaxies from the *JWST*-PRIMAL archival study (Heintz et al. 2025, grey markers and scatter points), selected at $z > 3$ and with $\text{H}\beta$ detections with $\text{S/N} > 3$. The metallicities of these galaxies were obtained using strong-line calibrations from Sanders et al. (2024) and Laseter et al. (2024), using a joint χ^2 approach taking into account each strong-line ratio available (\bar{R} , Ne3O2 , R3 , R2 , R23 ,

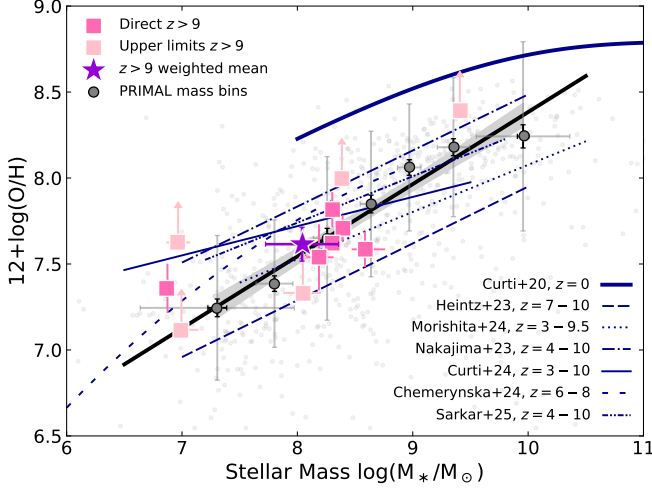


Fig. 6. Mass-metallicity relation at $z > 9$. Direct T_e metallicities and lower limits for the $z > 9$ sample are shown in hot pink and light pink respectively, with the weighted mean and 1σ error of the sample indicated by the purple star. Various mass-metallicity relations from literature are plotted (Heintz et al. 2023a; Curti et al. 2020; Morishita et al. 2024; Nakajima et al. 2023; Curti et al. 2024; Chemerynska et al. 2024). Light grey scatter points represent the PRIMAL $z = 3 - 10$ sample, with grey circular markers and their associated solid black error bars being the median and 1σ error of stellar mass bins. The grey error bars represent the standard deviation of mass bins. The bold solid black line shows the best fit to the PRIMAL stellar-mass bins.

O32), inversely weighted by its intrinsic scatter.

$$\chi^2(x) = \sum_n \frac{(R_{obs,n} - R_{cal,n}(x))^2}{\sigma_{obs,n}^2 + \sigma_{cal,n}^2} \quad (1)$$

Where $x = 12 + \log(\text{O}/\text{H})$, R_{obs} is the observed line ratio with error σ_{obs} , R_{cal} is the modelled line ratio, and σ_{cal} is the reported scatter of the diagnostic (Curti et al. 2020).

We divide 735 galaxies into 7 stellar-mass bins of 105 galaxies each, and fit a simple log-linear relation to the bins (solid black line), with a best-fit relation of $12 + \log(\text{O}/\text{H}) = (0.42 \pm 0.04) \log_{10}(M_*) + (4.19 \pm 0.34)$. The weighted mean of our T_e -based sample (depicted by a purple star) lies in line with the derived relation for the PRIMAL galaxies.

4.4. Deviation from the fundamental-metallicity relation

The MZR has been observed to have an additional dependence on the SFR, with highly star-forming galaxies appearing to be more metal-poor at a given stellar mass. To reduce the scatter on the MZR, Mannucci et al. (2010) introduced the fundamental metallicity relation (FMR) with an additional parametrisation for SFR;

$$\mu_\alpha = \log_{10} M_* - \alpha \times \log_{10}(\text{SFR}) \quad (2)$$

Where α is a constant between 0 and 1, chosen to minimise the scatter in $\mu_\alpha - Z$ space (Mannucci et al. 2010; Andrews & Martini 2013). The FMR appears universally constant out to $z \approx 3$ (Sanders et al. 2021), though recent *JWST* measurements report a break from this relation for the highest redshift galaxies (Heintz et al. 2023a; Nakajima et al. 2023; Curti et al. 2024) with the exact transition period still debated (likely between $z \approx 4 - 8$). In Figure 7, we compare our sample with early *JWST* results from Heintz et al. (2023a), and mass-redshift bins from (Curti

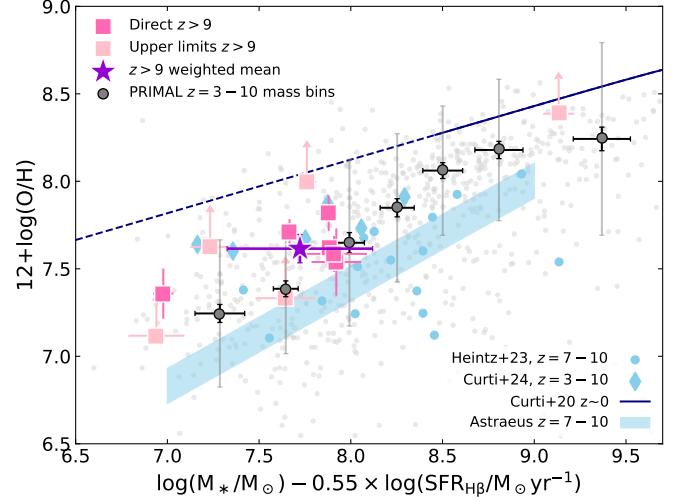


Fig. 7. The Fundamental Metallicity Relation at $z > 9$. Direct T_e metallicities and upper limits for the $z > 9$ sample are shown in hot pink and light pink respectively, with the weighted mean of the sample indicated by the purple star. The local FMR (Curti et al. 2020) is plotted in dark blue, and extrapolated to lower μ_α . Grey scatter points represent the PRIMAL $z = 3 - 10$ sample, with grey markers being the median of stellar mass bins. The solid black and grey error bars on these points represent the error on the median, and standard deviation of each bin respectively. We compare to previous high- z *JWST* results with diamonds from Curti et al. (2024), circles from Heintz et al. (2023a). The blue shaded region shows predictions from the Astraeus simulations for $z = 7 - 10$.

et al. 2024), as well as the predicted FMR from the Astraeus simulation at $z = 7 - 10$ (Ucci et al. 2023). As background, we show the full PRIMAL sample at $z = 3 - 10$ with metallicities based on the strong-line diagnostics. The weighted mean of our sample is 0.4 dex below the extrapolated FMR for galaxies in the local Universe. It is generally consistent with the underlying PRIMAL high-redshift *JWST* sample, that overall indicate a slightly steeper slope of $\alpha = 0.78$ than determined locally ($\alpha = 0.32 - 0.65$; Mannucci et al. 2010; Andrews & Martini 2013; Curti et al. 2020).

In Figure 8, we compile the high-redshift observations and show the overall evolution of the FMR with redshift. We calculate the offset from the local FMR, using the parametrisation outlined in Curti et al. (2020) (Equation 5; $\alpha = 0.56$). As seen in Fig. 7, the majority of the $z = 9$ sample lie in a M_* -SFR regime which the low- z galaxies do not cover, where the FMR has been extrapolated. However, local high- z analogue samples that probe lower μ_α do appear to follow the expected FMR (e.g. Arellano-Córdova et al. 2024, follows Andrews & Martini (2013); Curti et al. (2020)). We observe a systematic break from the local FMR for galaxies at $z \geq 3$, potentially evolving from -0.25 dex at $z = 3$ down to -0.7 dex at $z > 6$. The weighted mean of the $z = 9 - 10$ sample is offset by 0.4 dex from the local relation, consistent with other *JWST* studies (Heintz et al. 2023a; Curti et al. 2024; Roberts-Borsani et al. 2024; Scholte et al. 2025). These observations indicate substantially different physical properties driving galaxy growth within the first Gyr of cosmic time. We will interpret and discuss potential scenarios to explain the observed deviations from the FMR in more detail in Sect. 5 below.

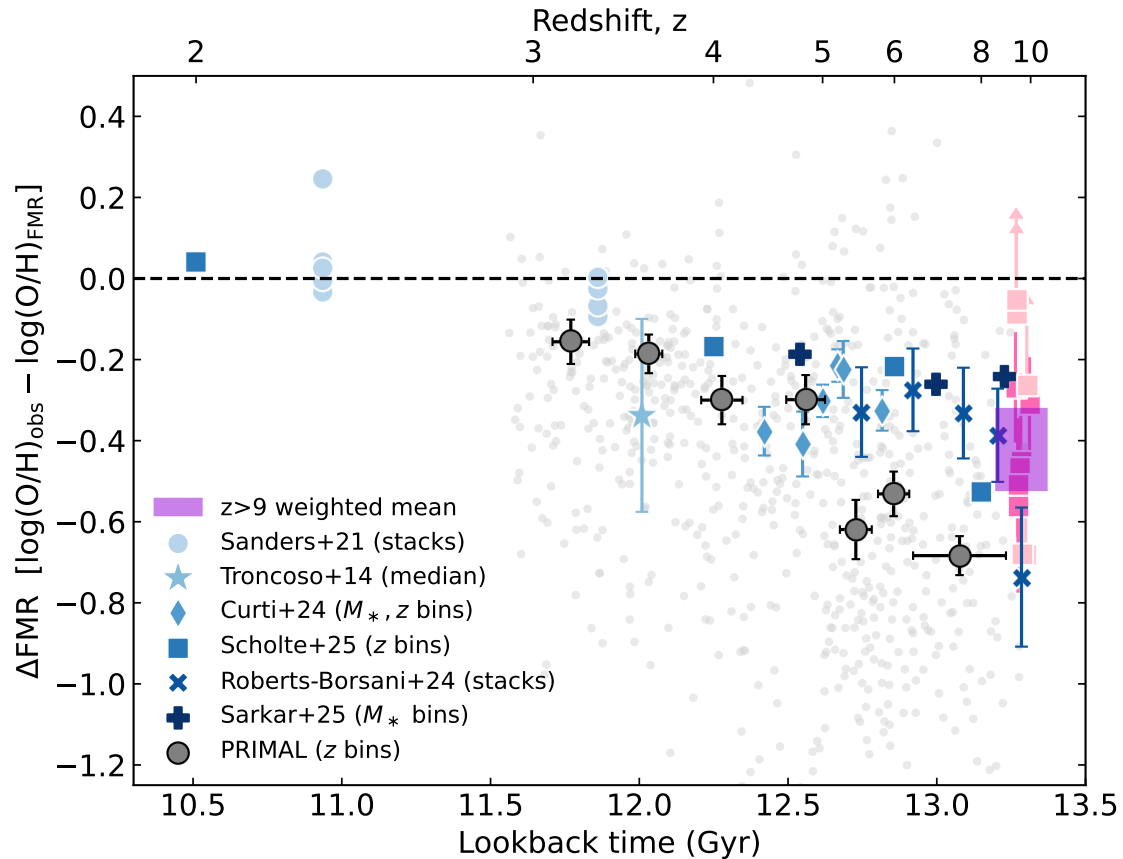


Fig. 8. Offset from the FMR, plotted against lookback time and redshift, down to $z \sim 2$. The weighted mean of $z > 9$ direct-metallicity sample is shown by the purple box, with height and width spanning 1σ error, and individual galaxies are plotted in pink. We compare to redshift bins of the PRIMAL $z = 3 - 10$ sample, shown as grey circular markers, with errorbars representing the error on the bin medians. Other binned or stacked high- z ($z > 2$) literature data are shown in different shades of blue, from Sanders et al. (2021); Troncoso et al. (2014); Curti et al. (2024); Scholte et al. (2025); Roberts-Borsani et al. (2024); Sarkar et al. (2025). There is a clear trend indicating that the offset from the FMR increases with redshift, with a systematic break somewhere between $2.5 < z < 3.0$.

5. Discussion – Uncovering the epoch of galaxy assembly via pristine gas infall?

There is now mounting evidence for a potential transition in the physics governing galaxy growth at high redshifts (Heintz et al. 2023a; Nakajima et al. 2023; Curti et al. 2024), as indicated by the break from the otherwise fundamental-metallicity relation. Previous observations found that this relation was constant out to $z \approx 3$ (Sanders et al. 2021), during the majority of cosmic time over the last 12 Gyr. The break to lower metallicities at high-redshifts has been interpreted as a signpost of chemical ‘dilution’ due to excessive pristine gas inflows (Heintz et al. 2023a), as also indicated by the higher fraction of strong Lyman- α H I absorbers in galaxies at these redshifts (e.g., Heintz et al. 2024, 2025; Umeda et al. 2023; D’Eugenio et al. 2024; Hainline et al. 2024; Witstok et al. 2024).

Indeed, Li et al. (2025b) proposed an analytical model describing the break from the FMR towards lower metallicities and found that dilution from excessive pristine gas accretion was favoured over feedback or outflow effects. Heintz et al. (2022) also found observational evidence for the bulk of the intergalactic H I gas being accreted in galaxy halos by $z \sim 2 - 3$ by comparing the build-up of the H I gas mass in the ISM to the global H I gas mass density inferred from quasar absorbers (see e.g., Walter et al. 2020, and references therein). Observations of gas-selected quasar absorption-line galaxies show a sharp break at

$z = 2.6 \pm 0.2$ in the metallicity evolution with redshift of the sample (Møller et al. 2013), argued to signal the transition in the mode of galaxy growth due to the starvation of primordial gas infall.

While these complementary results seem to support the physical scenario where the offset in the FMR is primarily driven by the physical transition of galaxies being fed new pristine gas via inflows, there are also potential alternative explanations. Liu et al. (2025) proposed that the observed high- z FMR can be constructed with a more efficient formation of high-mass ($m_{\text{max}} > 200 M_{\odot}$) stars following a “top-heavy” initial mass function (IMF). Interestingly, Cullen et al. (2025) find that a top-heavy IMF or other more exotic stellar populations are required to explain the extremely low metallicity of EXCELS-63107. Strong outflows, as expected for high sSFRs ($> 25 \text{ Gyr}^{-1}$) like we observe here, may also expel the dust and metals from the galaxies (Ferrara 2024; Pallottini et al. 2024), which could also explain the overabundance of bright UV galaxies at $z \gtrsim 10$. However, we do not see any prominent signatures of high-mass star formation in our sample, such as nitrogen overabundances, nor any broad emission-line “wings” indicative of outflows.

Instead, we argue that the most likely explanation for the offset from the FMR at $z \gtrsim 3$ is representing an excessive pristine gas inflows onto galaxies, which eventually become infall starved and evolve in a near-equilibrium state, mainly re-processing previously acquired gas at later cosmic times. Intriguing

ingly, the peak of cosmic star formation occurs at $z \sim 2$ (Madau & Dickinson 2014), approximately 800 Myr after the transition at $z = 2.6$, similar to the typical gas depletion times of star-forming galaxies at early cosmic epochs (Tacconi et al. 2018; Dessauges-Zavadsky et al. 2020; Aravena et al. 2024). This suggests that for the galaxies now being found in abundance and characterized in detail with *JWST* at $z \gtrsim 3$, we are directly witnessing their formation in progress.

6. Conclusion & future outlook

In this work, we characterized in detail the rest-frame UV and optical properties of a sample of galaxies at $z = 9.3 - 10.0$, with the main goal to determine their direct metallicities. This is enabled based on the updated reduction and data processing pipeline of *JWST*/NIRSpec Prism spectroscopic observations, as part of the 4th version of DJA (see Heintz et al. 2025; de Graaff et al. 2024, for previous releases), extending the wavelength coverage to $5.5\mu\text{m}$. Our sample included new observations from major *JWST* legacy surveys such as CAPERS, RUBIES, UNCOVER, and JADES. Due to the extended wavelength coverage and increasing spectral resolution with wavelength delivered by the NIRSpec Prism configuration, we were able to resolve the auroral [O III] $\lambda 4363$ line emission and compare to other rest-frame optical line transitions such as the [O III] $\lambda\lambda 4959, 5007$ doublet out to $z = 10$. This provided the first direct constraints on the metallicity, ionisation state, and electron temperatures for a sizeable sample of galaxies at $z \approx 10$.

Overall, we found that the sample galaxies were characterized by line ratios indicating strong ISM radiation fields compared to their local galaxy counterparts, with typical electron temperatures $T_e \gtrsim 2 \times 10^4$ K. The derived metallicities were on average 10% of solar, ranging from $12 + \log(\text{O}/\text{H}) = 7.1$ to 8.3. We found good agreement between existing high-redshift strong-line diagnostics in the literature (e.g., Sanders et al. 2024) and our sample, suggesting that these are universally valid at $z = 3 - 10$. We further derived an empirical relation connecting the direct metallicities to the UV brightness, M_{UV} , of the targets, valuable to estimate the metallicity for the much more numerous population of galaxies at $z \gtrsim 10$ only covered by *JWST* photometry.

We modelled the rest-frame UV to optical SED of each galaxy with BAGPIPES (Carnall et al. 2019) to determine their basic physical properties such as the SFR and stellar mass. Jointly with the emission-line analysis, we found evidence for bursty star formation with the SFR on 10 Myr to 100 Myr timescale on average being $\text{SFR}_{10}/\text{SFR}_{100} \approx 2$. The SFR-stellar mass main sequence and the mass-metallicity relation of the sample galaxies at $z \approx 10$ were consistent with expectations based on lower-redshift observations, indicating only a mild evolution from $z \approx 6$ to 10. Intriguingly, we found significant evidence for a systematic offset of -0.41 ± 0.10 dex from the fundamental-metallicity relation (e.g., Mannucci et al. 2010; Curti et al. 2020) at $z \approx 10$, supported also by the larger PRIMAL sample (Heintz et al. 2025), though based on strong-line calibrations for the metallicities. This indicates that pristine gas infall drives the overall star formation history of the Universe.

To push the current redshift frontier of T_e -based metallicity measurements, *JWST*'s MIRI spectroscopic capabilities could be fully utilised to cover the redshifted auroral and nebular emission lines at $z \approx 10$ (e.g., Hsiao et al. 2024b; Zavala et al. 2025). The lower sensitivity of MIRI means this would require a large time investment; however it remains our only instrument capable of covering the necessary rest-optical lines above $z \approx 10$.

These lines will remain out of reach for next-generation telescope such as the ESO Extremely Large Telescope (ELT), which will instead provide a substantial improvement in spectral resolving power, allowing more detailed characterizations of the rest-frame UV features at $z \gtrsim 10$, which are key to understand the nebular densities and temperatures of the star-forming regions of galaxies at cosmic dawn.

Acknowledgements. We express our greatest gratitude to the investigators on the major *JWST* observing programs, such as RUBIES, CAPERS, UNCOVER, and JADES. The work presented here would not have been possible without their major efforts in designing and obtaining the observational data included in our work here. The Cosmic Dawn Center (DAWN) is funded by the Danish National Research Foundation under grant DNRF140. The data products presented herein were retrieved from the DAWN *JWST* Archive (DJA). DJA is an initiative of the Cosmic Dawn Center, which is funded by the Danish National Research Foundation under grant DNRF140. This work has received funding from the Swiss State Secretariat for Education, Research and Innovation (SERI) under contract number MB22.00072, as well as from the Swiss National Science Foundation (SNSF) through project grant 200020_207349. This work is based in part on observations made with the NASA/ESA/CSA James Webb Space Telescope. The data were obtained from the Mikulski Archive for Space Telescopes (MAST) at the Space Telescope Science Institute, which is operated by the Association of Universities for Research in Astronomy, Inc., under NASA contract NAS 5-03127 for *JWST*.

References

- Abdurro'uf, Larson, R. L., Coe, D., et al. 2024, *ApJ*, 973, 47, doi: [10.3847/1538-4357/ad6001](#)
- Aggarwal, K. M., & Keenan, F. P. 1999, *ApJS*, 123, 311, doi: [10.1086/313232](#)
- Aihara, H., Allende Prieto, C., An, D., et al. 2011, *ApJS*, 193, 29, doi: [10.1088/0067-0049/193/2/29](#)
- Andrews, B. H., & Martini, P. 2013, *ApJ*, 765, 140, doi: [10.1088/0004-637X/765/2/140](#)
- Aravena, M., Heintz, K., Dessauges-Zavadsky, M., et al. 2024, *A&A*, 682, A24, doi: [10.1051/0004-6361/202347281](#)
- Arellano-Córdova, K. Z., Berg, D. A., Chisholm, J., et al. 2022, *ApJ*, 940, L23, doi: [10.3847/2041-8213/ac9ab2](#)
- Arellano-Córdova, K. Z., Cullen, F., Carnall, A. C., et al. 2024, arXiv e-prints, arXiv:2412.10557, doi: [10.48550/arXiv.2412.10557](#)
- Asplund, M., Grevesse, N., Sauval, A. J., & Scott, P. 2009, *ARA&A*, 47, 481, doi: [10.1146/annurev.astro.46.060407.145222](#)
- Atek, H., Shuntov, M., Furtak, L. J., et al. 2023, *MNRAS*, 519, 1201, doi: [10.1093/mnras/stac3144](#)
- Austin, D., Conselice, C. J., Adams, N. J., et al. 2024, arXiv e-prints, arXiv:2404.10751, doi: [10.48550/arXiv.2404.10751](#)
- Backhaus, B. E., Cleri, N. J., Trump, J. R., et al. 2025, arXiv e-prints, arXiv:2502.03519, doi: [10.48550/arXiv.2502.03519](#)
- Baker, W. M., Maiolino, R., Belfiore, F., et al. 2023, *MNRAS*, 518, 4767, doi: [10.1093/mnras/stac3413](#)
- Baldwin, J. A., Phillips, M. M., & Terlevich, R. 1981, *PASP*, 93, 5, doi: [10.1086/130766](#)
- Berg, D. A., Chisholm, J., Erb, D. K., et al. 2021, *ApJ*, 922, 170, doi: [10.3847/1538-4357/ac141b](#)
- Bezanson, R., Labbe, I., Whitaker, K. E., et al. 2022, arXiv e-prints, arXiv:2212.04026, doi: [10.48550/arXiv.2212.04026](#)
- . 2024, *ApJ*, 974, 92, doi: [10.3847/1538-4357/ad66cf](#)
- Boydett, K., Bunker, A. J., Curtis-Lake, E., et al. 2024, *MNRAS*, 535, 1796, doi: [10.1093/mnras/stae2430](#)
- Brammer, G. 2023, msaexp: NIRSpec analysis tools, 0.6.17, Zenodo, Zenodo, doi: [10.5281/zenodo.7299500](#)
- Brinchmann, J., Charlot, S., White, S. D. M., et al. 2004, *MNRAS*, 351, 1151, doi: [10.1111/j.1365-2966.2004.07881.x](#)
- Bunker, A. J., Cameron, A. J., Curtis-Lake, E., et al. 2023, arXiv e-prints, arXiv:2306.02467, doi: [10.48550/arXiv.2306.02467](#)
- Byler, N., Dalcanton, J. J., Conroy, C., & Johnson, B. D. 2017, *ApJ*, 840, 44, doi: [10.3847/1538-4357/aa6c66](#)
- Calabrò, A., Pentericci, L., Santini, P., et al. 2024, *A&A*, 690, A290, doi: [10.1051/0004-6361/202449768](#)
- Calzetti, D., Armus, L., Bohlin, R. C., et al. 2000, *ApJ*, 533, 682, doi: [10.1086/308692](#)
- Cameron, A. J., Katz, H., Witten, C., et al. 2024, *MNRAS*, 534, 523, doi: [10.1093/mnras/stae1547](#)
- Carnall, A. C., McLure, R. J., Dunlop, J. S., & Davé, R. 2018, *MNRAS*, 480, 4379, doi: [10.1093/mnras/sty2169](#)

- Carnall, A. C., McLure, R. J., Dunlop, J. S., et al. 2019, MNRAS, 490, 417, doi: [10.1093/mnras/stz2544](#)
- Castellano, M., Fontana, A., Treu, T., et al. 2023, ApJ, 948, L14, doi: [10.3847/2041-8213/accea5](#)
- Cataldi, E., Belfiore, F., Curti, M., et al. 2025, arXiv e-prints, arXiv:2504.03839, doi: [10.48550/arXiv.2504.03839](#)
- Chemerynska, I., Atek, H., Dayal, P., et al. 2024, ApJ, 976, L15, doi: [10.3847/2041-8213/ad8dc9](#)
- Cole, J. W., Papovich, C., Finkelstein, S. L., et al. 2025, ApJ, 979, 193, doi: [10.3847/1538-4357/ad9a6a](#)
- Cullen, F., McLeod, D. J., McLure, R. J., et al. 2024, MNRAS, 531, 997, doi: [10.1093/mnras/stae1211](#)
- Cullen, F., Carnall, A. C., Scholte, D., et al. 2025, arXiv e-prints, arXiv:2501.11099, doi: [10.48550/arXiv.2501.11099](#)
- Curti, M., Mannucci, F., Cresci, G., & Maiolino, R. 2020, MNRAS, 491, 944, doi: [10.1093/mnras/stz2910](#)
- Curti, M., D'Eugenio, F., Carniani, S., et al. 2023, MNRAS, 518, 425, doi: [10.1093/mnras/stac2737](#)
- Curti, M., Maiolino, R., Curtis-Lake, E., et al. 2024, A&A, 684, A75, doi: [10.1051/0004-6361/202346698](#)
- Curti, M., Witstok, J., Jakobsen, P., et al. 2025, A&A, 697, A89, doi: [10.1051/0004-6361/202451410](#)
- Daddi, E., Dickinson, M., Morrison, G., et al. 2007, ApJ, 670, 156, doi: [10.1086/521818](#)
- de Graaff, A., Brammer, G., Weibel, A., et al. 2024, arXiv e-prints, arXiv:2409.05948, doi: [10.48550/arXiv.2409.05948](#)
- Dessauges-Zavadsky, M., Ginolfi, M., Pozzi, F., et al. 2020, A&A, 643, A5, doi: [10.1051/0004-6361/202038231](#)
- D'Eugenio, F., Maiolino, R., Carniani, S., et al. 2024, A&A, 689, A152, doi: [10.1051/0004-6361/202348636](#)
- Díaz, A. I., Castellanos, M., Terlevich, E., & Luisa García-Vargas, M. 2000, MNRAS, 318, 462, doi: [10.1046/j.1365-8711.2000.03737.x](#)
- Dottorini, D., Calabrò, A., Pentericci, L., et al. 2024, arXiv e-prints, arXiv:2412.01623, doi: [10.48550/arXiv.2412.01623](#)
- Eisenstein, D. J., Willott, C., Alberts, S., et al. 2023a, arXiv e-prints, arXiv:2306.02465, doi: [10.48550/arXiv.2306.02465](#)
- Eisenstein, D. J., Johnson, B. D., Robertson, B., et al. 2023b, arXiv e-prints, arXiv:2310.12340, doi: [10.48550/arXiv.2310.12340](#)
- Ellison, S. L., Patton, D. R., Simard, L., & McConnachie, A. W. 2008, AJ, 135, 1877, doi: [10.1088/0004-6256/135/5/1877](#)
- Endsley, R., Chisholm, J., Stark, D. P., Topping, M. W., & Whittler, L. 2024, arXiv e-prints, arXiv:2410.01905, doi: [10.48550/arXiv.2410.01905](#)
- Erb, D. K., Shapley, A. E., Pettini, M., et al. 2006, ApJ, 644, 813, doi: [10.1086/503623](#)
- Ferland, G. J., Chatzikos, M., Guzmán, F., et al. 2017, Rev. Mexicana Astron. Astrofís., 53, 385, doi: [10.48550/arXiv.1705.10877](#)
- Ferrara, A. 2024, A&A, 684, A207, doi: [10.1051/0004-6361/202348321](#)
- Froese Fischer, C., & Tachiev, G. 2004, Atomic Data and Nuclear Data Tables, 87, 1, doi: [10.1016/j.adt.2004.02.001](#)
- Fujimoto, S., Wang, B., Weaver, J., et al. 2023, arXiv e-prints, arXiv:2308.11609, doi: [10.48550/arXiv.2308.11609](#)
- Furtak, L. J., Zitrin, A., Weaver, J. R., et al. 2023, MNRAS, 523, 4568, doi: [10.1093/mnras/stad1627](#)
- Garnett, D. R. 1992, AJ, 103, 1330, doi: [10.1086/116146](#)
- Gelli, V., Mason, C., & Hayward, C. C. 2024, ApJ, 975, 192, doi: [10.3847/1538-4357/ad7b36](#)
- Giménez-Arteaga, C., Oesch, P. A., Brammer, G. B., et al. 2023, ApJ, 948, 126, doi: [10.3847/1538-4357/acc5ea](#)
- Hainline, K. N., D'Eugenio, F., Jakobsen, P., et al. 2024, arXiv e-prints, arXiv:2404.04325, doi: [10.48550/arXiv.2404.04325](#)
- Harikane, Y., Sanders, R. L., Ellis, R., et al. 2025, arXiv e-prints, arXiv:2505.09186, doi: [10.48550/arXiv.2505.09186](#)
- Heintz, K. E., Oesch, P. A., Aravena, M., et al. 2022, ApJ, 934, L27, doi: [10.3847/2041-8213/ac8057](#)
- Heintz, K. E., Brammer, G. B., Giménez-Arteaga, C., et al. 2023a, Nature Astronomy, doi: [10.1038/s41550-023-02078-7](#)
- Heintz, K. E., Giménez-Arteaga, C., Fujimoto, S., et al. 2023b, ApJ, 944, L30, doi: [10.3847/2041-8213/acb2cf](#)
- Heintz, K. E., Watson, D., Brammer, G., et al. 2024, Science, 384, 890, doi: [10.1126/science.adj0343](#)
- Heintz, K. E., Brammer, G. B., Watson, D., et al. 2025, A&A, 693, A60, doi: [10.1051/0004-6361/202450243](#)
- Higson, E., Handley, W., Hobson, M., & Lasenby, A. 2019, Statistics and Computing, 29, 891, doi: [10.1007/s11222-018-9844-0](#)
- Horne, K. 1986, PASP, 98, 609, doi: [10.1086/131801](#)
- Hsiao, T. Y.-Y., Abdurro'uf, Coe, D., et al. 2023, arXiv e-prints, arXiv:2305.03042, doi: [10.48550/arXiv.2305.03042](#)
- . 2024a, ApJ, 973, 8, doi: [10.3847/1538-4357/ad5da8](#)
- Hsiao, T. Y.-Y., Álvarez-Márquez, J., Coe, D., et al. 2024b, ApJ, 973, 81, doi: [10.3847/1538-4357/ad6562](#)
- Isobe, Y., Ouchi, M., Nakajima, K., et al. 2023, ApJ, 956, 139, doi: [10.3847/1538-4357/acf376](#)
- Jakobsen, P., Ferruit, P., Alves de Oliveira, C., et al. 2022, A&A, 661, A80, doi: [10.1051/0004-6361/202142663](#)
- Katz, H., Cameron, A. J., Saxena, A., et al. 2024, arXiv e-prints, arXiv:2408.03189, doi: [10.48550/arXiv.2408.03189](#)
- Kewley, L. J., & Ellison, S. L. 2008, ApJ, 681, 1183, doi: [10.1086/587500](#)
- Kewley, L. J., Nicholls, D. C., & Sutherland, R. S. 2019, ARA&A, 57, 511, doi: [10.1146/annurev-astro-081817-051832](#)
- Kisielius, R., Storey, P. J., Ferland, G. J., & Keenan, F. P. 2009, MNRAS, 397, 903, doi: [10.1111/j.1365-2966.2009.14989.x](#)
- Kokorev, V., Chávez Ortiz, Ó. A., Taylor, A. J., et al. 2025, arXiv e-prints, arXiv:2504.12504, doi: [10.48550/arXiv.2504.12504](#)
- Koposov, S., Speagle, J., Barbary, K., et al. 2022, joshspeagle/dynesty: v2.0.3, v2.0.3, Zenodo, doi: [10.5281/zenodo.7388523](#)
- Lange, J. U. 2023, MNRAS, 525, 3181, doi: [10.1093/mnras/stad2441](#)
- Langeroodi, D., Hjorth, J., Chen, W., et al. 2023, ApJ, 957, 39, doi: [10.3847/1538-4357/acdbcl](#)
- Laseter, I. H., Maseda, M. V., Curti, M., et al. 2024, A&A, 681, A70, doi: [10.1051/0004-6361/202347133](#)
- Lee, H., Skillman, E. D., Cannon, J. M., et al. 2006, ApJ, 647, 970, doi: [10.1086/505573](#)
- Lee, N., Sanders, D. B., Casey, C. M., et al. 2015, ApJ, 801, 80, doi: [10.1088/0004-637X/801/2/80](#)
- Leja, J., Carnall, A. C., Johnson, B. D., Conroy, C., & Speagle, J. S. 2019, ApJ, 876, 3, doi: [10.3847/1538-4357/ab133c](#)
- Lequeux, J., Peimbert, M., Rayo, J. F., Serrano, A., & Torres-Peimbert, S. 1979, A&A, 80, 155
- Li, S., Wang, X., Chen, Y., et al. 2025a, ApJ, 979, L13, doi: [10.3847/2041-8213/ad9eac](#)
- Li, Z., Kakiichi, K., Christensen, L., et al. 2025b, arXiv e-prints, arXiv:2504.18616, doi: [10.48550/arXiv.2504.18616](#)
- Lilly, S. J., Carollo, C. M., Pipino, A., Renzini, A., & Peng, Y. 2013, ApJ, 772, 119, doi: [10.1088/0004-637X/772/2/119](#)
- Liu, B., Mapelli, M., Bromm, V., et al. 2025, arXiv e-prints, arXiv:2506.06139, doi: [10.48550/arXiv.2506.06139](#)
- Luridiana, V., Morisset, C., & Shaw, R. A. 2015, A&A, 573, A42, doi: [10.1051/0004-6361/201323152](#)
- Madau, P., & Dickinson, M. 2014, ARA&A, 52, 415, doi: [10.1146/annurev-astro-081811-125615](#)
- Maiolino, R., & Mannucci, F. 2019, A&A Rev., 27, 3, doi: [10.1007/s00159-018-0112-2](#)
- Mannucci, F., Cresci, G., Maiolino, R., Marconi, A., & Gnerucci, A. 2010, MNRAS, 408, 2115, doi: [10.1111/j.1365-2966.2010.17291.x](#)
- Mazzolari, G., Übler, H., Maiolino, R., et al. 2024, A&A, 691, A345, doi: [10.1051/0004-6361/202450407](#)
- Møller, P., Fynbo, J. P. U., Ledoux, C., & Nilsson, K. K. 2013, MNRAS, 430, 2680, doi: [10.1093/mnras/stt067](#)
- Morishita, T., Stiavelli, M., Grillo, C., et al. 2024, ApJ, 971, 43, doi: [10.3847/1538-4357/ad5290](#)
- Nakajima, K., Ouchi, M., Isobe, Y., et al. 2023, arXiv e-prints, arXiv:2301.12825, doi: [10.48550/arXiv.2301.12825](#)
- Nakajima, K., Ouchi, M., Xu, Y., et al. 2022, ApJS, 262, 3, doi: [10.3847/1538-4365/ac7710](#)
- Narayanan, D., Lower, S., Torrey, P., et al. 2024, ApJ, 961, 73, doi: [10.3847/1538-4357/ad0966](#)
- Osterbrock, D. E., & Ferland, G. J. 2006, Astrophysics of gaseous nebulae and active galactic nuclei
- Pallottini, A., Ferrara, A., Gallerani, S., et al. 2024, arXiv e-prints, arXiv:2408.00061, doi: [10.48550/arXiv.2408.00061](#)
- Peimbert, M., Peimbert, A., & Delgado-Inglada, G. 2017, PASP, 129, 082001, doi: [10.1088/1538-3873/aa72c3](#)
- Pérez-Montero, E. 2017, PASP, 129, 043001, doi: [10.1088/1538-3873/aa5abb](#)
- Planck Collaboration, Aghanim, N., Akrami, Y., et al. 2020, A&A, 641, A6, doi: [10.1051/0004-6361/201833910](#)
- Price, S. H., Bezanson, R., Labbe, I., et al. 2025, ApJ, 982, 51, doi: [10.3847/1538-4357/adaec1](#)
- Roberts-Borsani, G., Treu, T., Chen, W., et al. 2023, Nature, 618, 480, doi: [10.1038/s41586-023-05994-w](#)
- Roberts-Borsani, G., Treu, T., Shapley, A., et al. 2024, arXiv e-prints, arXiv:2403.07103, doi: [10.48550/arXiv.2403.07103](#)
- Rowland, L. E., Stefanon, M., Bouwens, R., et al. 2025, arXiv e-prints, arXiv:2501.10559, doi: [10.48550/arXiv.2501.10559](#)
- Salim, S., Boquien, M., & Lee, J. C. 2018, ApJ, 859, 11, doi: [10.3847/1538-4357/aabf3c](#)

- Salim, S., & Narayanan, D. 2020, *ARA&A*, 58, 529, doi: [10.1146/annurev-astro-032620-021933](https://doi.org/10.1146/annurev-astro-032620-021933)
- Sanders, R. L., Shapley, A. E., Topping, M. W., Reddy, N. A., & Brammer, G. B. 2024, *ApJ*, 962, 24, doi: [10.3847/1538-4357/ad15fc](https://doi.org/10.3847/1538-4357/ad15fc)
- Sanders, R. L., Shapley, A. E., Kriek, M., et al. 2016, *ApJ*, 816, 23, doi: [10.3847/0004-637X/816/1/23](https://doi.org/10.3847/0004-637X/816/1/23)
- Sanders, R. L., Shapley, A. E., Jones, T., et al. 2021, *ApJ*, 914, 19, doi: [10.3847/1538-4357/abf4c1](https://doi.org/10.3847/1538-4357/abf4c1)
- Sarkar, A., Chakraborty, P., Vogelsberger, M., et al. 2025, *ApJ*, 978, 136, doi: [10.3847/1538-4357/ad8f32](https://doi.org/10.3847/1538-4357/ad8f32)
- Saxena, A., Bunker, A. J., Jones, G. C., et al. 2024, *A&A*, 684, A84, doi: [10.1051/0004-6361/202347132](https://doi.org/10.1051/0004-6361/202347132)
- Schaerer, D., Marques-Chaves, R., Barrufet, L., et al. 2022, *A&A*, 665, L4, doi: [10.1051/0004-6361/202244556](https://doi.org/10.1051/0004-6361/202244556)
- Scholte, D., Cullen, F., Carnall, A. C., et al. 2025, arXiv e-prints, arXiv:2502.10499, doi: [10.48550/arXiv.2502.10499](https://doi.org/10.48550/arXiv.2502.10499)
- Shapley, A. E., Reddy, N. A., Sanders, R. L., Topping, M. W., & Brammer, G. B. 2023a, *ApJ*, 950, L1, doi: [10.3847/2041-8213/acd939](https://doi.org/10.3847/2041-8213/acd939)
- Shapley, A. E., Sanders, R. L., Reddy, N. A., Topping, M. W., & Brammer, G. B. 2023b, *ApJ*, 954, 157, doi: [10.3847/1538-4357/acea5a](https://doi.org/10.3847/1538-4357/acea5a)
- Speagle, J. S. 2020, *MNRAS*, 493, 3132, doi: [10.1093/mnras/staa278](https://doi.org/10.1093/mnras/staa278)
- Speagle, J. S., Steinhardt, C. L., Capak, P. L., & Silverman, J. D. 2014, *ApJS*, 214, 15, doi: [10.1088/0067-0049/214/2/15](https://doi.org/10.1088/0067-0049/214/2/15)
- Stanway, E. R., & Eldridge, J. J. 2018, *MNRAS*, 479, 75, doi: [10.1093/mnras/sty1353](https://doi.org/10.1093/mnras/sty1353)
- Steinhardt, C. L., Kokorev, V., Rusakov, V., Garcia, E., & Sneppen, A. 2023, *ApJ*, 951, L40, doi: [10.3847/2041-8213/acdef6](https://doi.org/10.3847/2041-8213/acdef6)
- Strait, V., Brammer, G., Muzzin, A., et al. 2023, *ApJ*, 949, L23, doi: [10.3847/2041-8213/acd457](https://doi.org/10.3847/2041-8213/acd457)
- Sun, G., Faucher-Giguère, C.-A., Hayward, C. C., et al. 2023, *ApJ*, 955, L35, doi: [10.3847/2041-8213/acf85a](https://doi.org/10.3847/2041-8213/acf85a)
- Tacconi, L. J., Genzel, R., Saintonge, A., et al. 2018, *ApJ*, 853, 179, doi: [10.3847/1538-4357/aaa4b4](https://doi.org/10.3847/1538-4357/aaa4b4)
- Thorne, J. E., Robotham, A. S. G., Davies, L. J. M., et al. 2021, *MNRAS*, 505, 540, doi: [10.1093/mnras/stab1294](https://doi.org/10.1093/mnras/stab1294)
- Topping, M. W., Stark, D. P., Endsley, R., et al. 2022, *MNRAS*, 516, 975, doi: [10.1093/mnras/stac2291](https://doi.org/10.1093/mnras/stac2291)
- . 2024, *MNRAS*, 529, 4087, doi: [10.1093/mnras/stae800](https://doi.org/10.1093/mnras/stae800)
- Topping, M. W., Sanders, R. L., Shapley, A. E., et al. 2025, arXiv e-prints, arXiv:2502.08712, doi: [10.48550/arXiv.2502.08712](https://doi.org/10.48550/arXiv.2502.08712)
- Tremonti, C. A., Heckman, T. M., Kauffmann, G., et al. 2004, *ApJ*, 613, 898, doi: [10.1086/423264](https://doi.org/10.1086/423264)
- Troncoso, P., Maiolino, R., Sommariva, V., et al. 2014, *A&A*, 563, A58, doi: [10.1051/0004-6361/201322099](https://doi.org/10.1051/0004-6361/201322099)
- Trump, J. R., Arrabal Haro, P., Simons, R. C., et al. 2023, *ApJ*, 945, 35, doi: [10.3847/1538-4357/acba8a](https://doi.org/10.3847/1538-4357/acba8a)
- Ucci, G., Dayal, P., Hutter, A., et al. 2023, *MNRAS*, 518, 3557, doi: [10.1093/mnras/stac2654](https://doi.org/10.1093/mnras/stac2654)
- Umeda, H., Ouchi, M., Nakajima, K., et al. 2023, arXiv e-prints, arXiv:2306.00487, doi: [10.48550/arXiv.2306.00487](https://doi.org/10.48550/arXiv.2306.00487)
- Valentino, F., Brammer, G., Gould, K. M. L., et al. 2023, *ApJ*, 947, 20, doi: [10.3847/1538-4357/acbefa](https://doi.org/10.3847/1538-4357/acbefa)
- Valentino, F., Heintz, K. E., Brammer, G., et al. 2025, arXiv e-prints, arXiv:2503.01990, doi: [10.48550/arXiv.2503.01990](https://doi.org/10.48550/arXiv.2503.01990)
- Walter, F., Carilli, C., Neeleman, M., et al. 2020, *ApJ*, 902, 111, doi: [10.3847/1538-4357/abb82e](https://doi.org/10.3847/1538-4357/abb82e)
- Whitaker, K. E., van Dokkum, P. G., Brammer, G., & Franx, M. 2012, *ApJ*, 754, L29, doi: [10.1088/2041-8205/754/2/L29](https://doi.org/10.1088/2041-8205/754/2/L29)
- Williams, H., Kelly, P. L., Chen, W., et al. 2023, *Science*, 380, 416, doi: [10.1126/science.adf5307](https://doi.org/10.1126/science.adf5307)
- Witstok, J., Smit, R., Maiolino, R., et al. 2021, *MNRAS*, 508, 1686, doi: [10.1093/mnras/stab2591](https://doi.org/10.1093/mnras/stab2591)
- Witstok, J., Jakobsen, P., Maiolino, R., et al. 2024, arXiv e-prints, arXiv:2408.16608, doi: [10.48550/arXiv.2408.16608](https://doi.org/10.48550/arXiv.2408.16608)
- Zavala, J. A., Castellano, M., Akins, H. B., et al. 2025, *Nature Astronomy*, 9, 155, doi: [10.1038/s41550-024-02397-3](https://doi.org/10.1038/s41550-024-02397-3)
- Zitrin, A., Zheng, W., Broadhurst, T., et al. 2014, *ApJ*, 793, L12, doi: [10.1088/2041-8205/793/1/L12](https://doi.org/10.1088/2041-8205/793/1/L12)